Redox-influenced seismic properties of upper-mantle olivine

C. J. Cline II[1]*, U. H. Faul[2], E. C. David[1†], A. J. Berry[1], I. Jackson[1]

[1]*Research School of Earth Sciences, Australian National University, Canberra, Australia*

[2]*Earth Atmospheric and Planetary Sciences, Massachusetts Institute of Technology, Cambridge, MA, USA*

Lateral variations of seismic wave speeds and attenuation (dissipation of strain energy) in the Earth's upper mantle have the potential to map key characteristics such as temperature, major-element composition, melt fraction, and water content[1-3]. The inversion of this data into meaningful representations of physical properties requires a robust understanding of the micromechanical processes that affect the propagation of seismic waves[2,3]. Structurally bound water (hydroxyl) is believed to significantly affect seismic properties[2,3] - however, this has yet to be experimentally quantified. Here we present the first comprehensive low-frequency assessment of the seismic properties of olivine as a function of water content within the geophysically relevant under-saturated regime. Our results demonstrate that wave speeds and attenuation are in fact strikingly insensitive to water content. Rather, the imposed redox conditions and associated defect chemistry appear to have a substantial influence on the seismic properties. These findings suggest that elevated water contents are not responsible for low velocity/high attenuation structures in the upper mantle. Instead, high attenuation observed in hydrous and oxidized regions of the upper mantle (e.g. above subduction zones) may reflect the prevailing oxygen fugacity (fO_2). Additionally, the new data provide no support for the hypothesis whereby a sharp lithosphere-asthenosphere boundary is explained by enhanced grain boundary sliding in the presence of water.

† Current address: Department of Earth Sciences, University College London, London, UK

Lattice defects and the structure/composition of grain boundaries in olivine strongly influence the stiffness and strength of the mantle from infinitesimal strains (elastic/anelastic)[4-6], to large-strain viscous rheology[7]. Central to experimental efforts in quantifying these effects is understanding the influence of hydrogen-related defects on both diffusional and dislocation-governed processes[8,9]. It has been suggested, mainly by analogy with observations of water-enhanced viscous deformation of olivine, that the potential seismological significance of water in the mantle might involve either an increase in defect mobility through increased vacancy populations, or water-enhanced diffusivities facilitating grain boundary sliding[2,10,11] . Substantially modified seismic properties in the presence of water have been observed previously at low frequencies, but only in a single exploratory study conducted under water-saturated conditions[12]. Accordingly, hypotheses concerning water-enhanced grain boundary sliding as an explanation for the sharp lithosphere-asthenosphere boundary[10,11], and the more general seismological mapping of mantle water contents[2], remain to be experimentally tested.

Water is conventionally introduced into experimental specimens through the use of solid buffers containing hydrated phases[9], or as excess fluid, ensuring high water fugacity (fH_2O) and water-saturated conditions during mechanical testing[9,12]. However, free fluid phases are not expected under upper mantle conditions. Conducting experiments under a more relevant water-undersaturated environment requires conditions sufficiently oxidizing to ensure that $fH_2O > fH_2$ (see online methods), for the decoration of intrinsic and extrinsic defects with H^+. A recent experimental campaign[13] utilized the energetically favored Ti-clinohumite-like defect ('Ti-OH')[14-16] (Ti located on a metal-site, charge balanced by a doubly protonated Si-vacancy) to assess the sensitivity of large-strain creep in olivine to small (and undersaturated) water concentrations. A conspicuous modification of large-strain rheology was observed in the presence of low concentrations of this defect, with a near-linear enhancement of strain

rate in dislocation creep occurring as a function of increasing hydroxyl content, inferred to be due to the increased concentration of associated Si vacancies[13].

Motivated by the scant experimental data on the influence of water on seismic properties, here we build upon the study by (ref. 13) to explore for the first time the micro-strain anelastic effects of changes in fO_2 and fH_2O, conducive to the formation of water-undersaturated conditions. We isostatically hot-pressed, and then mechanically tested under a range of fO_2 conditions, eight polycrystalline olivine specimens containing different types of hydrated defects in various concentrations. We used different metal sleeves surrounding the olivine specimen during testing to vary the imposed redox conditions[13] - either Pt to create relatively oxidizing conditions, Ni_{70}/Fe_{30} ('NiFe') for more reducing conditions, or Ni for an intermediate fO_2. The sample suite consists of undoped and Ti-doped Fo_{90} solgel olivine[13], Ti-doped forsterite, and a reconstituted San Carlos olivine (see **Extended data Table 1** for sample compositions). Each specimen was mechanically tested in torsional forced-oscillation at periods representative of the seismic band (1-1000 s), using a confining pressure of 200 MPa and temperatures up to 1200 °C (further details are available in the online methods section).

Fourier-transform infrared (FTIR) spectroscopy was used to identify and quantify the water content of each specimen after mechanical testing. The FTIR spectra (**Fig. 1a)** of Ti-bearing specimens are dominated by absorption bands at 3572 and 3525 cm^{-1}, attributed to the Ti-OH defect[14,15], for which a site-specific calibration factor[16] was used to infer the concentration of chemically bound OH. The residual broadband absorbance is attributed to the presence of molecular water, and higher concentrations of molecular water are prominent in Ti-free specimens. Additional hydrated defects associated with Si vacancies (at wavenumber 3612 cm^{-1}) and trivalent ions (at wavenumber 3350 cm^{-1}) can also be observed in some specimens.

The specimen tested within a NiFe-sleeve shows no absorbance within the range 4000-3000 cm^{-1}, indicating the absence of both chemically bound hydroxyl and molecular water.

Mechanical data from all specimens exhibit anelastic relaxation typical of the 'absorption band': a monotonic increase of dissipation (Q^{-1}) and decrease of shear modulus (G) with increasing oscillation period (**Fig. 1b** and **1c**) and with increasing temperature. Further, the (G,Q^{-1}) data for each specimen can be adequately described by a Burgers-type creep function[17]. Previous forced oscillation results for a Pt-encapsulated and water-saturated dunite[12] show a broad similarity in shear modulus and dissipation to the similarly sleeved, but water-undersaturated, specimens of this study. Additionally, the global Burgers model[17] for a suite of dry and melt-free Fo_{90} polycrystals, updated to fit additional more recent data, closely matches those for the Ti-doped NiFe-sleeved sample tested here, thus indicating that the presence of the Ti-dopant alone does not affect the observed anelastic relaxation (**Fig. 1b**).

The dissipation, and associated frequency dependence (dispersion) of the shear modulus, are markedly enhanced for the Fe-bearing olivine specimens tested within Pt sleeves relative to the specimen tested within NiFe (**Fig. 1b & 1c**). However, within the suite of Pt-sleeved Fe-bearing polycrystals, the mechanical behavior is strikingly consistent for specimens ranging widely in concentrations of both bound hydroxyl associated with Ti (**Fig. 2a**). It is therefore concluded that the anelastic behavior of olivine does not vary systematically with either [H/Si], or Si-vacancies associated with the Ti-OH defect, in contrast to the findings of (ref. 13) regarding water-enhanced large strain dislocation creep. In addition, the presence of varying quantities of molecular water (**Fig. 2b**) and other hydrated defect species also appears to have no consequence for the measured seismic properties. Finally, despite the presence of structural water associated with Ti/Mg substitution and Si vacancies, the mechanical properties of the Ti-doped forsterite sample are indistinguishable from those of dry, NiFe-

sleeved Fo_{90} olivine (**Fig. 1 & 2**) - suggesting that in the absence of Fe, higher fO_2 and fH_2O conditions are ineffective in enhancing anelastic relaxation.

The magnitude of anelastic relaxation of Fe-bearing olivine represented in **Fig. 1b** and **1c** instead correlates well with the prevailing fO_2, influenced by the respective metal sleeving materials. The fO_2 conditions were inferred from separate hot-pressing experiments, involving the measurement of Fe partitioning between olivine and widely dispersed fine-grained Pt blebs, and vary between Pt- and NiFe-sleeved solgel olivine specimens by 1.7 log units. The calculated values of fO_2 within our large specimens differ from those of the respective metal-oxide buffer, but the expected relative ordering is maintained amongst the different sleeving materials, e.g. Pt > Ni > NiFe (see online methods). Additionally, the fO_2 of Pt-sleeved San Carlos olivine is 0.9 log units higher than pure solgel olivine within Pt due to the presence of impurities, such as Ni and Cr[20]. Using the commonly invoked defect charge balance between the concentrations of ferric Fe [$Fe^{\bullet}_M$] and metal-site vacancies [V''_M][9,18,19], we find that Pt-sleeved specimens contain concentrations of such defects roughly twice as high as NiFe-sleeved specimens. The dissipation measured for the Fe-bearing olivine specimens across the entire range of temperatures and oscillation periods is consistent with the relation $Q^{-1} \sim (fO_2)^{1/3}$ (**Fig. 3**). Our data clearly demonstrate a previously unrecognized link between Q^{-1} and redox conditions. The strength of the inferred sensitivity to variation of fO_2 results from the relatively small range of fO_2 conditions prevailing in the interior of our large olivine charges sleeved in different metals.

Increased concentrations and mobilities of lattice defects resulting from more oxidizing conditions (specifically $Fe^{3+}$and vacancies on metal-sites), and associated increases in lattice and grain-boundary diffusivities, are the likely the cause of the observed enhancement in anelastic relaxation. Accordingly, under these more oxidizing conditions, the effective grain-boundary viscosity will be reduced, and hence also the characteristic timescales τ_e and τ_M

(the Maxwell time), associated with elastically, and diffusionally assisted/accommodated grain boundary sliding respectively[5]. Indeed, values of τ_M determined from the Burgers model fitting[17] of (G,Q^{-1}) data for each specimen vary systematically with fO_2 (**Fig. 4**). It has been suggested that water contents of 0.1 wt% may decrease τ_e by two to four orders of magnitude and thus enhance dissipation for elastically accommodated grain boundary sliding, potentially explaining the sharp lithosphere-asthenosphere boundary[10,11]. Here we have demonstrated that there exists no such sensitivity of seismic properties to the presence of water under our experimental conditions, but observe a comparable enhancement of anelastic relaxation attributable to an increase of fO_2 by 1.7 log units, and the concomitant defects.

Results from the recent NoMelt seismic experiment, which was conducted in 60 to 80 Ma old lithosphere in the central Pacific, away from ridges and hotspots[21], are consistent with our findings of a negligible influence of water on seismic properties. Analyses of basalts from the East Pacific Rise and Macquarie Island indicate that water contents for the Pacific upper mantle approach 200 wt. ppm H_2O (ref. 22, and references therein). Taking partitioning of the bulk water content between olivine and pyroxenes into account, olivine in the upper mantle may thus contain ~ 400 - 1000 ppm H/Si[23,24] (i.e. within the range experimentally investigated here). In addition, electrical conductivity measurements collected as part of the NoMelt experiment indicate increased conductivity in the asthenosphere, consistent with water contents between 25 and 400 wt. ppm[25]. The presence of this amount of water was previously expected to substantially reduce seismic velocities[2,10]. However, the results of the NoMelt survey[21] indicate that the observed velocity structure, including the velocity minimum, can be explained with a relatively minor additional enhancement of the anelastic relaxation characteristics of dry and relatively reduced olivine[17], to a depth of 300 km, i.e. well below the melt (and volatile) extraction horizon (**Fig. 5**).

In contrast, the low velocity and high attenuation observed above subducting slabs are typically attributed to volatile release (thus higher water contents[26]), and to the presence of melt[3]. However, measurements of $Fe^{3+}/\Sigma Fe$ in arc lavas indicate fO_2 is also higher by 1-1.5 log units in the mantle wedge in comparison to beneath adjacent oceanic lithosphere[27-29]. With the $Q^{-1} \sim (fO_2)^{1/3}$ result of this study, such variations of fO_2 are predicted to enhance dissipation 2-3 fold with associated dispersion reflected in reduced wave speeds. Therefore, although water content generally correlates with magmatic ratios of $Fe^{3+}/\Sigma Fe$[(27)], and may also increase grain size[3], the reduced velocities and increased attenuation above subducting slabs may be attributable not to the presence of fluids or hydrated defects, but rather to the prevailing redox conditions and the presence of melt (**Fig. 5)**.

References

1 Romanowicz, B. A. & Mitchell, B. J. Deep Earth Structure: Q of the Earth from Crust to Core. Treatise on Geophysics (Second Edition) 789-827 (Elsevier, 2015).

2 Karato, S. Mapping water content in upper mantle. *Geophys. Monogr. AGU* **138**, 135-152 (2003).

3 Abers, G. *et al.* Reconciling mantle attenuation-temperature relationships from seismology, petrology, and laboratory measurements. *Geochem. Geophys.***15**, 3521-3542 (2014).

4 Jacobsen, S. D. *et al.* Effects of hydration on the elastic properties of olivine. *Geophys. Res. Lett.* **35**, L14303, doi:10.1029/2008GL034398 (2008).

5 Jackson, I. Properties of Rocks and Minerals: Physical Origins of Anelasticity and Attenuation in Rock. *Treatise on Geophysics (Second Edition)* 539-571 (Elsevier, 2015).

6 Farla, R. J., Jackson, I., Fitz Gerald, J. D., Faul, U. H. & Zimmerman, M. E. Dislocation damping and anisotropic seismic wave attenuation in Earth's upper mantle. *Science* **336**, 332-335, doi:10.1126/science.1218318 (2012).

7 Bai, Q., Mackwell, S. J. & Kohlstedt, D. L. High-temperature creep of olivine single crystals 1. Mechanical results for buffered samples. *J. Geophys. Res.* **96**, 2441, doi:10.1029/90jb01723 (1991).

8 Karato, S.-I. & Jung, H. Effects of pressure on high-temperature dislocation creep in olivine. *Philos. Mag.* **83**, 401-414, doi:10.1080/0141861021000025829 (2003).

9 Mei, S. & Kohlstedt, D. Influence of water on plastic deformation of olivine aggregates: 2. Diffusion creep regime. *J. Geophys. Res.* **105**, 21457-21469 (2000).

10 Karato, S.-I. On the origin of the asthenosphere. *Earth Planet. Sci. Lett.* **321**, 95-103 (2012).

11 Olugboji, T.M., Karato, S-I., & Park, J. Structures of the oceanic lithosphere-asthenosphere boundary: Mineral-physics modeling and seismological signatures. *Geochem. Geophys*. **14(4)**, 880-901, doi:10.1002/ggge.20086.

12 Aizawa, Y. *et al.* Seismic properties of Anita Bay dunite: an exploratory study of the influence of water. *J. Petrol.* **49**, 841-855 (2008).

13 Faul, U. H., Cline II, C. J., David, E. C., Berry, A. J. & Jackson, I. Titanium-hydroxyl defect-controlled rheology of the Earth's upper mantle. *Earth Planet. Sci. Lett.* **452**, 227-237, doi:http://dx.doi.org/10.1016/j.epsl.2016.07.016 (2016).

14 Berry, A. J., Hermann, J., O'Neill, H. S. C. & Foran, G. J. Fingerprinting the water site in mantle olivine. *Geology* **33**, 869, doi:10.1130/g21759.1 (2005).

15 Walker, A. M., Hermann, J., Berry, A. J. & O'Neill, H. S. C. Three water sites in upper mantle olivine and the role of titanium in the water weakening mechanism. *J. Geophys. Res.***112**, doi:10.1029/2006jb004620 (2007).

16 Kovács, I., O'Neill, H. S. C., Hermann, J. & Hauri, H. Site-specific infrared OH absorption coefficients for water substitution into olivine. *Amer. Miner.* **95**, 292-299 (2010).

17 Jackson, I. & Faul, U. H. Grainsize-sensitive viscoelastic relaxation in olivine: Towards a robust laboratory-based model for seismological application. *Phys. Earth Planet. Inter.* **183**, 151-163, doi:10.1016/j.pepi.2010.09.005 (2010).

18 Nakamura, A. & Schmalzried, H. On the nonstoichiometry and point defects of olivine. *Phys. Chem. Miner.* **10**, 27-37, doi:10.1007/bf01204323 (1983).

19 Dohmen, R. & Chakraborty, S. Fe–Mg diffusion in olivine II: point defect chemistry, change of diffusion mechanisms and a model for calculation of diffusion coefficients in natural olivine. *Phys. Chem. Miner.* **34**, 409-430, doi:10.1007/s00269-007-0158-6 (2007).

20 De Hoog, J., Gail, L. & Cornell, D. Trace-element geochemistry of mantle olivine and application to mantle petrogenesis and geothermobarometry. *Chem Geol*. **270**, 196-215 (2010)

21 Lin, P.-Y. P. et al. High-resolution seismic constraints on flow dynamics in the oceanic asthenosphere. *Nature* **535**, 538-541, doi:10.1038/nature18012 (2016).

22 Shimizu, K. et al. Two-component mantle melting-mixing model for the generation of mid-ocean ridge basalts: implications for the volatile content of the Pacific upper mantle. *Geochim. Cosmochim. Acta* **176**, 44–80 (2016).

23 Hirth, G. & Kohlstedt, D. L. Water in the oceanic upper mantle: implications for rheology, melt extraction and the evolution of the lithosphere. *Earth Planet. Sci. Lett.* **144**, 93-108 (1996).

24 Tenner, T. J., Hirschmann, M. M., Withers, A. C., & Ardia, P. H_2O storage capacity of olivine and low-Ca pyroxene from 10 to 13 GPa: consequences for dehydration melting above the transition zone. *Contrib. Mineral. Petrol.,* **163**, 297-316 (2012).

25 Sarafian, E. et al. The electrical structure of the central Pacific upper mantle constrained by the NoMelt experiment. *Geochem. Geophys.* **16.4** 1115-1132 (2015).

26 Stachnik, J. C., Abers, G. A. & Christensen, D. H. Seismic attenuation and mantle wedge temperatures in the Alaska subduction zone. *J. Geophys. Res.***109** (2004).

27 Kelley, K. A. & Cottrell, E. Water and the Oxidation State of Subduction Zone Magmas. *Science* **325**, 605-607, doi:10.1126/science.1174156 (2009).

28 Brounce, M. N., Kelley, K. A. & Cottrell, E. Variations in $Fe^{3+}/\Sigma Fe$ of Mariana Arc Basalts and Mantle Wedge fO_2. *J. Petrol.* **55**, 2513-2536, doi:10.1093/petrology/egu065 (2014).

29 McCammon, C. A. et al. Oxidation state of iron in hydrous mantle phases: implications for subduction and mantle oxygen fugacity. *Phys. Earth Planet. Inter.* **143–144**, 157-169, doi:http://dx.doi.org/10.1016/j.pepi.2003.08.009 (2004).

Acknowledgments We thank Harri Kokkonen and Hayden Miller for technical support with sample preparation and operation of the ANU rock physics laboratory, in addition to Hua Chen for assistance with electron backscatter diffraction. Multiple conversations with Shun Karato greatly improved the manuscript, and are appreciated. This work was supported by grant DP130103848 from the Australian Research Council to I.J., A.J.B., U.F., and Shun Karato of Yale University. UF acknowledges support from NSF grant EAR 1321889. CJC gratefully acknowledges funding by an ANU International PhD Research Scholarship.

Author Contributions C.J.C. conducted the forced-oscillation measurements, with contributions from E.C.D.. C.J.C obtained the microstructural and spectroscopic data, subsequently interpreted by U.H.F., I.J., A.J.B and C.J.C. fO_2 and Fe^{3+} calculations were performed by U.H.F. The Manuscript was written by C.J.C. with contributing revisions and discussion from all authors.

Author information Reprints and permissions information is available at www.nature.com/reprints. The authors declare no competing financial interests. Correspondence and requests for materials should be addressed to C.J.C. (christopher.cline@anu.edu.au).

Main text figure legends

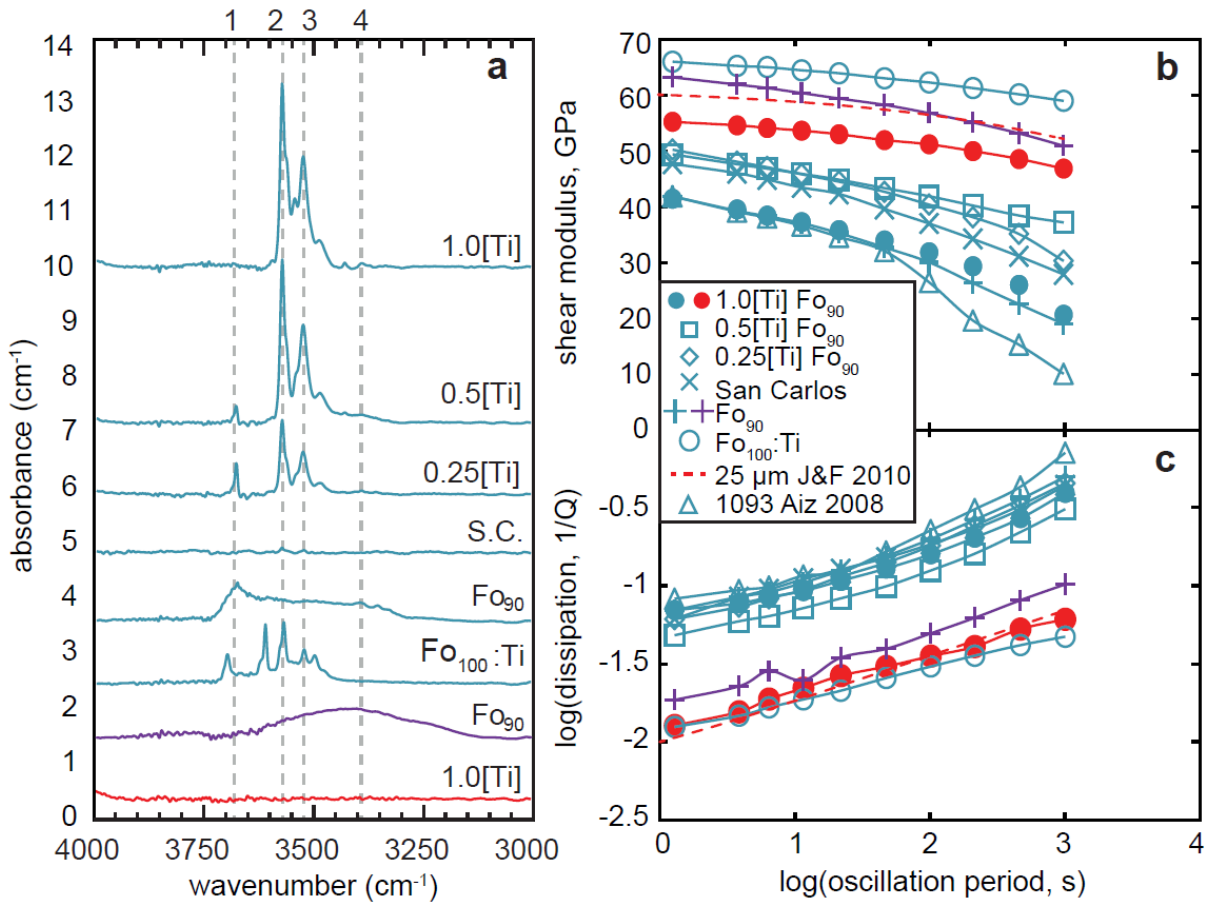

Figure 1: a, FTIR spectra for all specimens, with corresponding **b**, Shear modulus and **c,** dissipation data for a representative temperature of 1100 °C. Pt-sleeved specimens are represented by blue, Ni-sleeved by purple and NiFe-sleeved by red. Peaks labeled in **a,** represent (1) a secondary hydrous phase at wavenumber of 3690 cm^{-1}, (2-3) Ti-OH[14-16], (4) OH associated with trivalent ions[14,16]. The Burgers model for dry olivine[18] was evaluated for a grain size of 25 µm, and is shown by the red dashed curves. Data from a water-saturated Anita Bay dunite[12] are shown with blue triangles. Ti-doped samples are denoted by the nomenclature X[Ti] where X is the approximate amount of Ti normalized to the sample with the highest Ti-dopant concentration, i.e. 800 ppm Ti/Si (**Extended Data Table 1**). All experimental data are normalized to a common grain size of 25 µm[17].

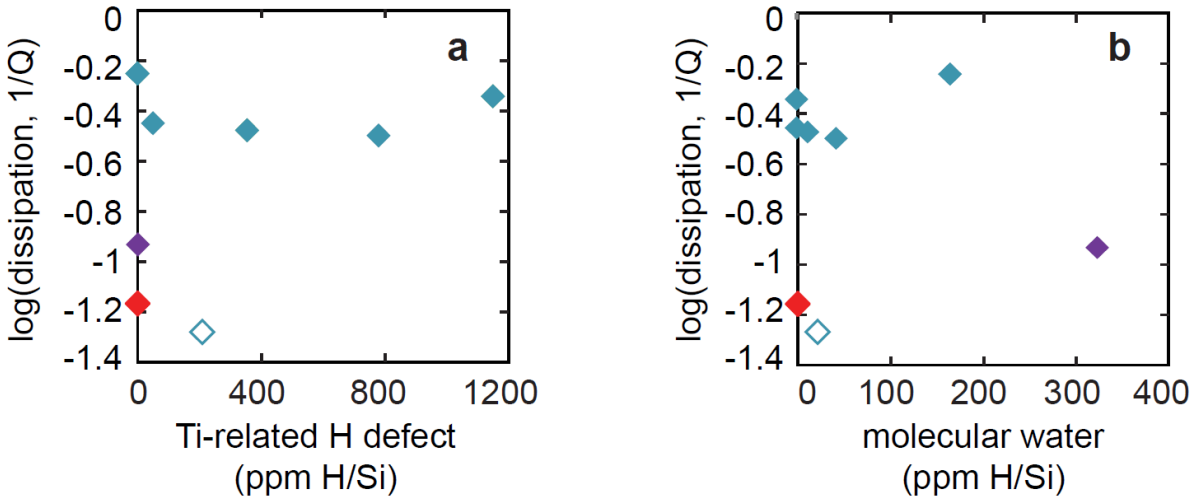

254

255 **Figure 2:** Dissipation measured at representative conditions (1100°C and 1000 s oscillation
256 period) for olivine specimens plotted against (a) the corresponding concentration of Ti-
257 related H and (b) the concentration of molecular water. Coloring scheme is the same as in
258 Fig. 1, with Fe-bearing olivine represented by solid symbols, and the Ti-doped forsterite
259 specimen represented by the hollow symbol. Dissipation data are normalized to a common
260 grain size of 25 μm. Errors on measurements of dissipation and water content are smaller
261 than the symbols used for plotting.

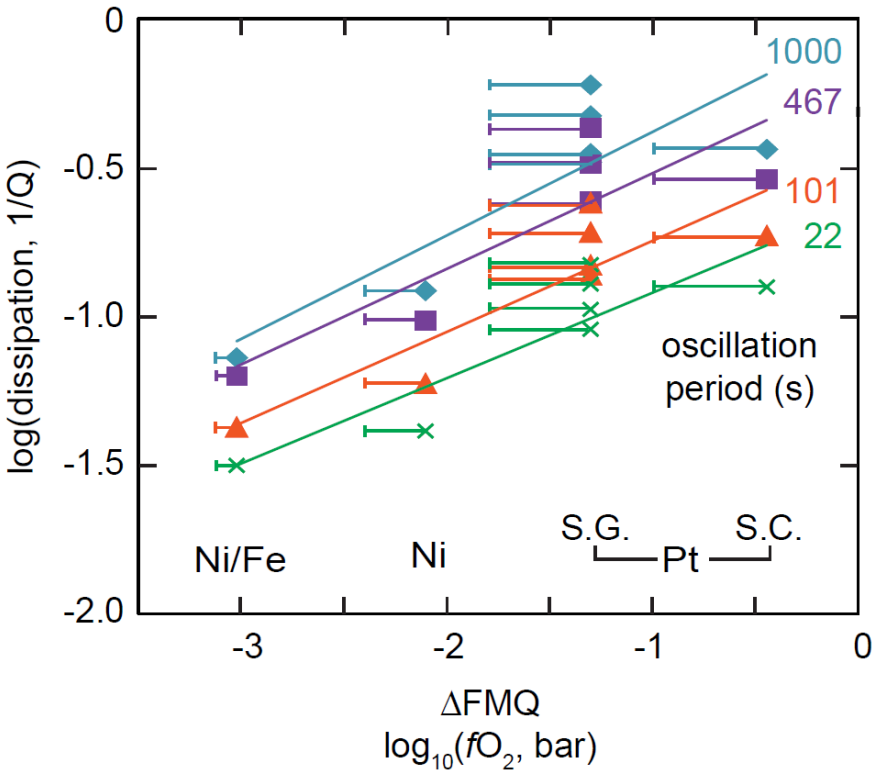

Figure 3: Dissipation data at 1100 °C plotted as a function of fO_2 determined for different capsule materials for several representative oscillation periods. Linear fits of the data at the various oscillation periods have an average slope of 0.31. Dissipation data are normalized to a common grain size 25 μm. Error bars on fO_2 measurements link values calculated using an alternative Fe-Pt activity-composition relationship, (see online methods section). S.G and S.C. represents solgel and San Carlos derived olivine specimens, respectively.

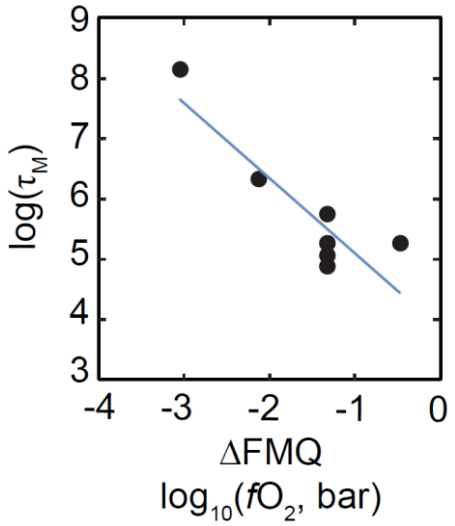

Figure 4: Values of log(τ_M) from the refined Burgers model of each Fo_{90} olivine specimen plotted as a function of corresponding redox condition. The data are best fit with a line of slope 1.2.

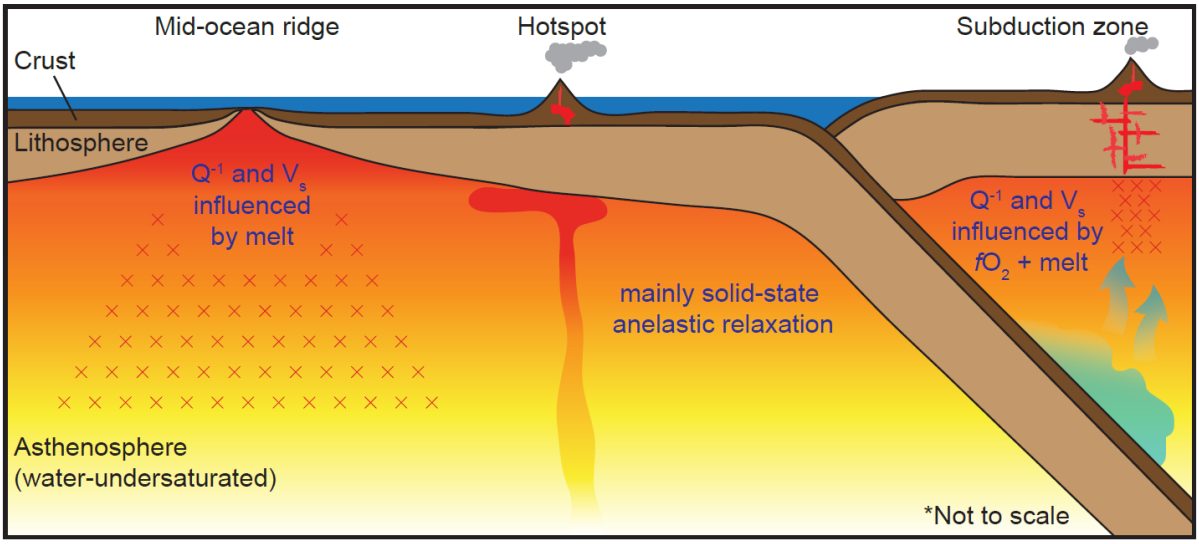

Figure 5: Dominant influences on anelastic relaxation responsible for the reduced seismic wave velocities and attenuation of seismic waves (listed in blue). 'Normal' asthenosphere beneath old oceanic lithosphere, which is water-undersaturated and contains only a very minor melt fraction, is subject mainly to solid-state anelastic relaxation. Higher melt fractions in mid-ocean ridge environments result in enhanced relaxation through the partial wetting of grain boundaries (red "X's" indicate the presence of appreciable melt), whereas mantle wedge environments are influenced by both the presence of melt and increased oxygen fugacity.

Methods

Specimen fabrication

Three types of starting materials were utilized to produce the eight olivine specimens tested in this study. Seven specimens were fabricated from precursor powder prepared by a solution-gelation process (two undoped Fo_{90}, four Ti-doped Fo_{90} and one Ti-doped Fo_{100}), and the other from powder produced by crushing hand-picked San Carlos olivine phenocrysts. The fabrication procedure for the different sol-gel derived olivine powders follows the methodology of (ref. 30) for Fo_{90}, and (ref. 13) for the Ti-doped forsterite material. Nitrates of Fe and Mg (and tetra-ethoxy orthotitanate for the Ti-bearing material) were mixed with a nonstoichiometric amount of tetraethyl orthosilicate to ensure that the final olivine was opx-saturated. Gelation of this mix was initiated with a small amount of HNO_3, followed by dehydration, and firing in air within a Pt crucible to remove all nitrate. The resulting powders were subjected to multiple firings in a 1 atmosphere furnace in a 50:50 CO-CO_2 gas mix, at 1400 °C for 16 h, with intervening grindings to produce a pure and homogeneous starting material with an average grain diameter ~ 1 μ m. The San Carlos precursor material is identical to that fabricated and used by (ref. 31).

The precursor powder was then cold-pressed at ~ 10 MPa into a set of five, 3 g pellets that were fired in an atmosphere of 50:50 CO-CO_2 for 16 h at either 1400 °C for the solgel, or 1300 °C for the San Carlos derived material. The stack of five pellets was accommodated within a laser-welded Pt capsule, sandwiched between alumina pistons within a thin-walled mild steel jacket and hot-pressed at 1200 °C and 300 MPa for 24 h in a Paterson internally-heated gas-medium pressure vessel. Specimens were recovered by dissolving the steel jacket in HNO_3 and subsequently peeling off the remaining Pt capsule. Transverse sections were cut ~ 1.5 from the end of each sample for microstructural analysis, with the bulk of the

specimens then being precision ground to a right cylindrical shape with a diameter of 11.5 mm and lengths ranging between 31 and 33 mm. Each such specimen was then fired at 600 °C in Ar to remove all traces of organic lubrication used in the grinding, and held in a drying oven at 110 °C until mechanical testing.

Mechanical testing

Mechanical testing of each specimen, via forced torsional oscillation, was conducted using the modified Paterson gas-medium apparatus originally described by (ref. 32), and later with updated procedures by (ref. 33). Specimens were sleeved in either Pt, $Ni_{70}Fe_{30}$ or Ni foil and placed inside of a mild-steel jacket along with Lucalox™ alumina torsion rods. Pressure was applied via Ar, and maintained at 200 MPa for the duration of the experiment to load all interfaces in the experimental assembly. The temperature was increased to 1200 °C, and maintained for a time interval ranging between 23 and 45 h, during which the mechanical response was monitored until steady and repeatable values of normalized compliance and phase lag were observed, indicating that the evolution of the microstructure and chemical environment is complete. Since this evolution will be thermally activated, once steady-state mechanical response is achieved at the highest temperature, continued mechanical testing during the slow staged cooling (over approximately 1 week) is thought to be representative of a single chemical environment and microstructure.

Torsional testing involves the application of a sinusoidal stress at each of 10 oscillation periods, logarithmically equi-spaced between 1 and 1000 s. Maximum strains at the highest temperature and longest oscillation period were kept to $< 10^{-5}$ to ensure linear behavior, which was confirmed before beginning the formal test at the highest temperature by halving the strain amplitude and monitoring values of Q^{-1}. A complete experiment encompasses testing at oscillation periods of 1-1000 s followed by a complimentary torsional microcreep test (ref. 32). After both types of torsional tests were complete, the temperature was dropped

by 50 °C, and the procedure repeated, continuing until nearly elastic behavior was observed, upon which the temperature interval was increased to 100 °C, until room temperature was reached.

Water content and grain size analysis

Water content was determined using Fourier-transform infrared spectroscopy (FTIR), for both the hot-pressed precursor- and specimens recovered after mechanical testing. Sections were thinned to 400 µm, then placed inside of a sealed Plexiglas box and purged with dry air for 45 minutes prior to, and continually during measurements. Spectra were recorded using a Bruker Hyperion 2000 microscope, utilizing a Tensor 27 spectrometer with MCT-A detector, and an aperture of 200 x 200 µm. Each measurement represents an average of 64 scans, recorded between 600 and 5000 cm^{-1} with a resolution of 4 cm^{-1}.

Determination of water content follows the method of (ref. 13), in which a site specific calibration factor of k = 0.18 is used to convert the integrated area between wavenumbers 3450 and 3600 cm^{-1} into the concentration of crystallographically bound hydroxyl. The residual broadband absorption, is attributed to the presence of molecular water[16], and is quantified separately using the magnitude of absorbance at wavenumber 3450 cm^{-1} and a molar absorption coefficient of 115 $Lmol^{-1}cm^{-1}$. An unidentified secondary hydrous phase identified in the FTIR spectra of some specimens will not affect the quoted water contents or the measured mechanical properties. Presumably this phase formed during the slow staged-cooling, Since hydrated phases are not stable >700 °C[(34)], and anelasticity is not appreciable or measurable below this temperature, these hydrous phases will not affect the mechanical response of the specimens. The presence of such a hydrous phase is suggestive of a hydrous environment during mechanical testing, even in the absence of any other structural H-related defects.

Electron back-scatter diffraction (EBSD) orientation maps were collected to determine the grain size of each specimen after mechanical testing. Sections were successively polished down from 800 grit silicon carbide to a final vibratory polish using 0.05 µm colloidal silica. Orientation maps were collected at the Center for Advanced Microscopy at ANU using a Zeiss Ultra Plus field-emission scanning electron microscope (FE-SEM) fitted with an Oxford Nordlys S EBSD camera. A representative orientation map is available in **Extended data Fig. 1**.

Determination of fO_2 and Fe^{3+} in olivine

The oxygen fugacity (fO_2) was determined for the differently sleeved olivine specimens through separate hot pressing experiments. 1 wt% Pt-black was mixed with either solgel or San Carlos derived olivine powder, then the material was encapsulated in either Pt, Ni, NiFe or Fe foil, and hot-pressed in a Paterson internally-heated gas apparatus at 1200 °C and 300 MPa for 24 hours. The recovered specimens were then analyzed using standardized EDS and electron microprobe WDS analysis to yield Fe contents of both the small Pt particles (~ 10 µm) and surrounding olivine. Using the metal activities (γ) in both the olivine and alloyed Pt-blebs, this then results in a calculable fO_2[35], using the relation[36]:

$$\log(fO_2) = 2\log(\gamma_{Fe}^{ol}) - 2\log(\gamma_{Fe}^{alloy}) + 2\log(X_{Fe}^{ol}/X_{Fe}^{alloy}) - \log(\alpha_{SiO2}) - \log(k_2),$$

where α_{SiO2} is silica activity, and X_{Fe} is the mole fraction of Fe either in the olivine or Pt-blebs. Earlier studies using a similar technique to determine fO_2 (e.g. ref. 36) utilized the activity relation provided from the work of (ref. 37), given as:

$$\gamma_{Fe}^{ol} = (1-X_{Fe}^{alloy})^2[-3.33+0.22(4X_{Fe}^{alloy})-1],$$

but the subsequent study of (ref. 35) addressed a variety of issues with this approach, including the exclusion of any temperature dependence of the activity coefficient. The

resultant activity-composition relationship provided by (ref. 35) is thus preferred for our measurements, and is given as:

$$\ln\gamma_{Fe}^{alloy} = [W_{G1} + 2(W_{G2} - W_{G1})\, X_{Fe}^{alloy}](\, X_{Pt}^{alloy})^2/RT,$$

where W_{G1} = 138 kJ/mol, W_{G2} = 90.8 kJ/mol, R is the gas constant and T is absolute temperature. Discrepancy between the fO_2 values calculated using the two described activity-compositions relationships increases as the concentration of Fe in the FePt blebs decreases (i.e. towards more oxidizing conditions), and can be observed by the error bars in **Fig. 3**. A detailed analysis of these additional hot-pressing experiments designed for the determination of fO_2 in large solid charges is currently being prepared for publication by authors U.H.F., C.J.C., I.J., and A.J.B..

The concentrations of Fe^{3+} $[Fe_M^{\bullet}]$, and through the charge neutrality conditions of olivine then concentration of metal-site vacancies $[V''_M]$, in our Pt and NiFe-sleeved specimens are assessed using eq. 3-5 of (ref.19, and references therein), using the appropriate fO_2 calculated above. Olivine at Si-saturated conditions (coexisting with pyroxene) possesses a concentration of Fe^{3+} defects described by:

$$\log[Fe_M^{\bullet}] = \frac{1}{6}\left(logK_x + 2log2 + 4logX_{Fa} + logf_{O_2} + loga_{SiO_2}\right)$$

where $\log K_x$ = -7.32- (90000/2.303RT)[21], T is in Kelvin, X_{Fa} is fayalite content. From this calculation of $[Fe^{\bullet}_M]$, the ratio of Fe^{3+} to total Fe can be accessed via the relation:

$$Fe^{3+}/\Sigma Fe = \frac{[Fe_M^{\bullet}]}{2X_{Fa}}$$

The calculated $\%Fe^{3+}$ of total Fe for interior of Pt-sleeved olivine is 0.17 in the interior. NiFe-sleeved specimens exhibit roughly half of this latter value at $\%Fe^{3+}$ = 0.09, and Ni-sleeved olivine is intermediate with 0.13.

Hydrogen speciation and water retention as a function of redox conditions

Water present in our forced-oscillation experiments is not intentionally added. The source of water is presumed to be either adsorption of moisture within the specimen following removal from the gas mixing furnace, and prior to pressurization, or ingress of H from the relatively reducing furnace environment into the more oxidizing environment within the specimen. Given the evident availability of H in our experiments, the presence of hydrated defects can be controlled through the use of different metal sleeving materials, imposing either favorable or unfavorable redox conditions for the oxidation of H.

The relative fugacities of H_2 and H_2O are controlled by the equilibrium $H_2 + ½O_2 = H_2O$ with an equilibrium constant K_w of 5.9 at 1200°C.[38]. Using the values of fO_2 determined from the separate hot-pressing experiments detailed above, the difference of +1.7 log units in fO_2 between NiFe- and Pt-sleeved olivine thus increases $fH_2O/fH_2 = K_w(fO_2,bar)^{1/2}$ from only 2.4 to 13.5 – consistent with the inferred dominance of oxidized hydrogen within Pt sleeves, and the loss of water as hydrogen from NiFe-sleeved olivine.

Additional references

30 Jackson, I. et al. Grain-size-sensitive seismic wave attenuation in polycrystalline olivine. *J. Geophys. Res.* **107**, doi:10.1029/2001jb001225 (2002).

31 Tan, B. H., Jackson, I. & Fitz Gerald, J. D. High-temperature viscoelasticity of fine-grained polycrystalline olivine. *Phys. Chem. Miner.* **28**, 641-664, doi:10.1007/s002690100189 (2001).

32 Jackson, I., Paterson, M. S. A high pressure, high temperature apparatus for studies of seismic wave dispersion and attenuation. *Pure Appl. Geophys.*. **141**, 375-406 (1993).

33 Jackson, I., Barnhoorn, A., Aizawa, Y. & Saint, C. Improved procedures for the laboratory study of high-temperature viscoelastic relaxation. *Phys. Earth Planet. Inter.* **172**, 104-115, doi:http://dx.doi.org/10.1016/j.pepi.2008.03.010 (2009).

34 Engi, M., Lindsley, D. H. Stability of titanian clinohumite: Experiments and thermodynamic analysis. *Contrib. Mineral. Petrol.* **72**, 415-424 (1980).

35 Kessel, R., Beckett, J. R. & Stolper, E. M. Thermodynamic properties of the Pt-Fe system. Amer. Miner. 86, 1003-1014 (2001).

36 Rubie, D. C., Karato, S., Yan, H. & O'Neill, H. S. C. Low differential stress and controlled chemical environment in multianvil high-pressure experiments. Phys. Chem. Miner. 20, 315-322, doi:10.1007/bf00215102 (1993).

37 Heald, E. Thermodynamics of iron-platinum alloys. Aime. Me.t Soc. Trans. 239, 1337-1340 (1967).

38 Paterson, M. The thermodynamics of water in quartz. Phys. Chem. Miner. 13, 245-255 (1986).

Extended data figure legends

Extended data Table 1: Summary of sample characteristics

Extended data

Table 1: Summary of sample characteristics

Sample	Precursor material	Normalized [Ti]*	Ti content	Metal sleeve	Bound hydroxyl ‡	Molecular water•	Grain size, µm§	ΔFMQ interior‖
1515	Fo_{90} Solgel	1	802(3.7)†	Pt	1150(190)	0	25.4	-1.3
1579	Fo_{90} Solgel	1	802(3.7)†	$Ni_{70}Fe_{30}$	0	0	25	-3.0
1623	Fo_{90} Solgel	0.5	396(0.5)†	Pt	780(36)	43	18.6	-1.3
1637	Fo_{90} Solgel	0.25	176(0.7)†	Pt	355(32)	12	19.9	-1.3
1646	San Carlos	N/A	18-46Δ	Pt	50(17)	0	80.9	-0.4
1651	Fo_{90} Solgel	0	0	Pt	0	167	20.6	-1.3
1684	Fo_{100} Solgel	1	800(5)	Pt	200(7)	23	8.2	-0.9
1689	Fo_{90} Solgel	0	0	Ni	0	327	10.7	-2.0

*Samples are denoted by the nomenclature X[Ti] where X is the amount normalized to the sample with the highest Ti-dopant concentration. The values of X correspond to the intended composition.
†Atom ppm Ti/Si determined by LA-ICPMS. Values in parenthesis are standard error (%).
‡Atom ppm H/Si by FTIR in the sample interior, associated with Ti-clinohumite-like defect only. Values in parenthesis indicate one standard deviation of data collected on longitudinal maps or (linear) transects.
•Atom ppm H/Si by FTIR in the sample interior, associated with molecular water concentration only.
§Calculated using EBSD orientation maps in combination with M-TEX processing software
‖In units of $\log_{10}(fO_2$, bar)
ΔFrom (ref. 20)

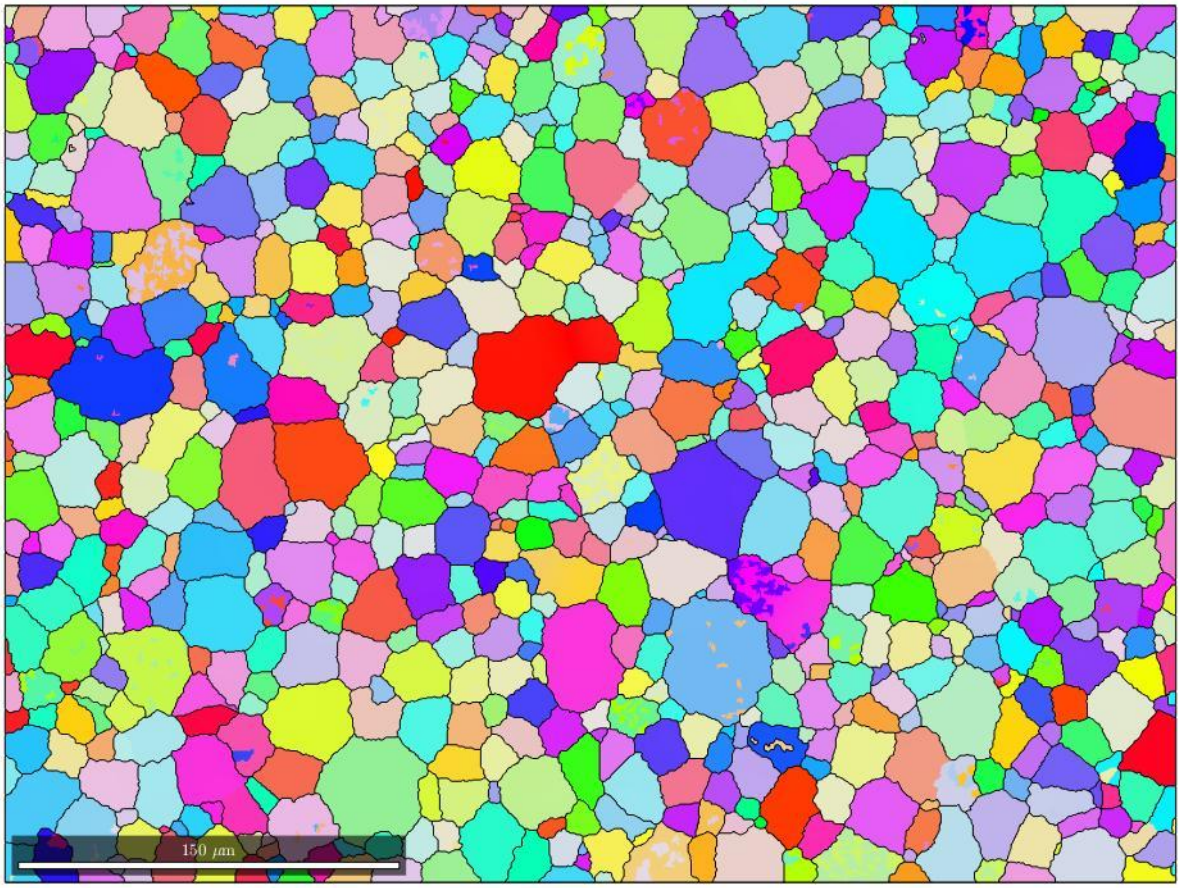

Extended data figure 1: EBSD map of sample 1623 (0.5[Ti]) after mechanical testing, colored to indicate crystallographic orientation. A near "foam" microstructure is present, with apparent grain boundary serrations being an artifact of the post-processing grain boundary reconstruction using MTEX.